



Full length article

In-situ synthesis via laser metal deposition of a lean Cu–3.4Cr–0.6Nb (at%) conductive alloy hardened by Cr nano-scale precipitates and by Laves phase micro-particles



Anoop R Kini^{a,*}, Dora Maischner^b, Andreas Weisheit^b, Dirk Ponge^a, Baptiste Gault^{a,c}, Eric A Jägle^{a,d}, Dierk Raabe^a

^a Department of Microstructure Physics and Alloy Design, Max-Planck-Institut für Eisenforschung GmbH, Max-Planck-Straße 1, 40237 Düsseldorf, Germany

^b Fraunhofer-Institut für Lasertechnik, Steinbachstraße 45, 52074 Aachen, Germany

^c Department of Materials, Royal School of Mines, Imperial College London, London, UK

^d Institut für Werkstoffkunde, Universität der Bundeswehr München, 85577 Neubiberg, Germany

ARTICLE INFO

Article history:

Received 16 February 2020

Revised 21 June 2020

Accepted 13 July 2020

Available online 16 July 2020

Keywords:

Additive manufacturing

Laser deposition

In-situ

Precipitation hardening

Atom probe tomography (APT)

ABSTRACT

Conductive and yet strong copper alloys are essential materials in highly mechanically loaded electrical devices. We demonstrate a novel in-situ synthesis approach via laser metal deposition (LMD) in a lean copper alloy, Cu–3.4Cr–0.6Nb (at%). Strengthening in the lean alloy comes from chromium nano-scale precipitates formed in-situ (4 nm diameter; number density $8 \times 10^{23} \text{ m}^{-3}$) and from Laves phase particles ($< 1 \mu\text{m}$ diameter; 2.2 vol%), dispersed across the microstructure. This dual dispersion, in a nearly pure copper matrix, is achieved through a suited combination of chromium alloying and cooling rate during LMD synthesis. The as-synthesized alloy has a conductivity of 68% IACS (International Annealed Copper Standard) and a Vickers hardness of 146, at room temperature. The latter is 11% above the value reported for the strongest lean reference ternary alloy Cu–8Cr–4Nb (at%). The in-situ synthesis approach averts any heat treatment step, which has been an essential step previously in conventional manufacturing, for realizing the property combination in lean Cu–Cr based system.

© 2020 Acta Materialia Inc. Published by Elsevier Ltd. All rights reserved.

1. Introduction

Conductive copper alloys which are also mechanically strong [1–3] are essential materials for high field pulsed magnets [1–4], direct current magnets [5], aerospace cables [6], rocket nozzle liners [7–9], robotics parts [1,3,10], circuit breaker parts and switchgears [11,12]. Achieving such a combination of properties is challenging because strengthening via alloying in copper compromises electrical/thermal conductivity. The latter is due to the scattering effects associated with solutes and interfaces [2,13,14]. One alloy design pathway has been the use of a low volume fraction of a second phase, through a low alloying amount. For instance, particle or precipitation hardened lean copper alloys [15,16]. Such alloys can have a tensile strength of up to 800 MPa and a conductivity of up to 84% IACS (International Annealed Copper Standard) [15,16].

The alloying elements used frequently are Cr [17], Ag [2,5], Zr [18], Nb [1,3,19], Ti [16], Fe [20], or their combination [3,6,10,21–23].

Even without alloying, exceptional strengthening in pure copper was demonstrated by inducing nano-twins in the microstructure by Lu et al. [24]. The material exhibited an excellent combination of conductivity (90% IACS) and tensile yield strength (800 MPa), at room temperature [24]. Nano-twinned pure copper, however, is restricted to service temperatures below 100 °C because of the limited thermal stability of the microstructure [24–26]. Above this temperature, lean copper alloys are technologically relevant materials.

One such material class is the lean Cu–Cr alloy system [15,27,28]. It has evolved into ternary systems with addition of either Ag [6,29], Zr [30,31], or Nb [8,14,32]. The Cu–Cr–Ag and Cu–Cr–Zr ternary systems rely mainly on coherent Cr precipitates [29,30,33] for strengthening. In the Cu–Cr–Ag system, the microstructures additionally include low volume fractions of Ag precipitate and Ag–Cu eutectic phase [1,6,34]. Likewise, alloys in the Cu–Cr–Zr system usually include Cu_4Zr and Cu_5Zr precipitates [30,31,33]. Upon conventional processing by rolling, these alloys

* Corresponding author.

E-mail addresses: anoopkini@gmail.com, anoop.maxplanck@gmail.com (A.R. Kini).

can reach a tensile strength of up to 670 MPa and a conductivity of up to 74 % IACS [33]. A post-process heat treatment step for aging has been indispensable to obtain the property combination in these lean ternary systems.

In Cu–Cr–Nb ternary system, Cu–8Cr–4Nb and Cu–4Cr–2Nb (at%) alloys [9,35] rely on Cr₂Nb Laves phase particles (< 1 µm in diameter; 7–14 vol%) for strengthening. Yet, they do not contain Cr precipitates. The Cr to Nb atomic ratio in these alloys has been 2:1, as the Cr content is fully consumed in the Cr₂Nb Laves phase particles, leaving behind a nearly pure copper matrix. This leads to a high conductivity of 54–76% IACS, along with a tensile yield strength of 200–280 MPa (Vickers hardness of up to 132) [9,35]. The reported property combination was obtained after a heat treatment step, demanding a minimum duration of 50 h at 1000 °C, following conventional extrusion processing. An alternative approach to strengthen alloys in the Cu–Cr–Nb system [36] is based on a microstructure with Cr incoherent precipitates along with a reduced volume fraction of Cr₂Nb Laves phase (about 2 vol%). This approach was illustrated in a Cu–2Cr–0.5Nb (at%) alloy [36], as processed by rapid solidification via melt spinning. A subsequent heat treatment step was not reported. It is unclear if, without heat treatment step, the strength and conductivity are both sufficient, as each of which has not been reported yet for this alloy variant in this ternary system.

Compared to the Cu–Cr–Ag and the Cu–Cr–Zr ternary systems, the Cu–Cr–Nb system bears advantages. First, Nb has a greater relative-abundance than Ag or Zr [37]. Second, the price of Nb (per weight) is mere 1/4th the price of Ag, and 1/10th the price of Zr. A drawback of Cu–Cr–Nb alloys, however, is the requirement for high processing temperatures as Nb steeply increases the melting temperatures of the alloys to about 1800 °C, even upon modest doping [14,32]. Also, Nb has poor oxidation resistance and has high reactivity, rendering the synthesis of alloys containing Nb to be challenging [38–40].

Laser additive manufacturing (LAM), a synthesis route based on rapid solidification [41], has recently driven endeavors to access new microstructures in alloys designed for high strength [42–45]. The key driver to obtain such microstructures has been a unique set of time-temperature profiles during and after solidification, including high thermal gradients along with high heating and cooling rates (> 10³ K/s) [44–46]. Specific to the ternary Cu–Cr–Nb system in the alloy variant Cu–8Cr–4Nb (at%), LAM was recently used to produce functional components with an analogous strength-conductivity property combination as those produced by cumbersome conventional manufacturing [47]. A post-LAM heat treatment step was essential that accompanied pressing [48].

Here, we demonstrate an in-situ synthesis approach via laser metal deposition (LMD) in a lean Cu–3.4Cr–0.6Nb (at%) alloy. In-situ refers to precipitation across the deposited material, considering the synthesis process step, as an event. A post-synthesis heat treatment process step is not necessary for this developed alloy, as it reaches a Vickers hardness of 146 and a conductivity of 68% IACS. The former is 11% above the value reported for the strongest lean reference ternary alloy Cu–8Cr–4Nb (at%) [9,35]. The alloy is hardened by in-situ Cr nano-scale precipitates, despite a low volume fraction of Laves phase particles (2.2 vol%). Microstructural characterization is performed and discussed in terms of precipitation kinetics under the influence of high in-process cooling rates during LMD.

2. Experimental details

2.1. Powder preparation

The alloy powders were produced by argon gas atomization at the Leibniz-Institut für Werkstofforientierte Technologien Bremen.

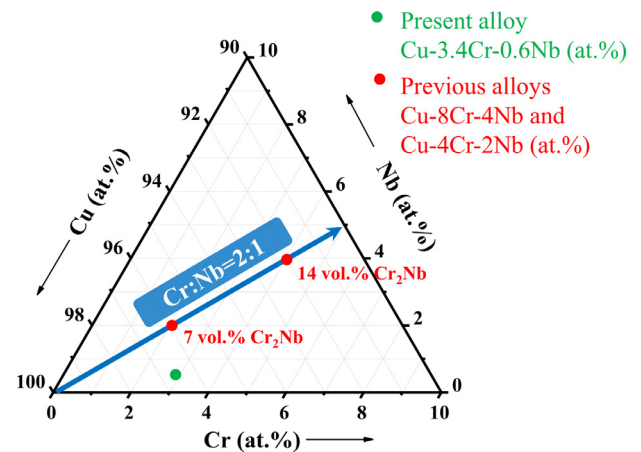


Fig. 1. The Cu–Cr–Nb compositional space shows the present Cu–3.4Cr–0.6Nb (at%) alloy. The alloy contains more Cr than that in Cr₂Nb Laves phase. Previously studied ternary alloys [9,35,49] are also indicated. (For the interpretation of colored labels in figures within the manuscript, the web version of the article must be referred.)

The alloy powder composition of Cu–3.4Cr–0.6Nb (at%) was verified by inductively coupled plasma optical emission spectrometry (ICP-OES). Fig. 1 shows the alloy composition in the ternary Cu–Cr–Nb space. The atomic ratio of alloying elements, i.e. Cr to Nb ratio, is greater than 2:1. The lever rule states the volume fraction of the Cr₂Nb Laves phase to be 2.2 vol%. This is a lower amount compared to the amounts in Cu–8Cr–4Nb (at%) and Cu–4Cr–2Nb (at%) alloys [9,35,49], as the Nb content is less. Fe in the alloy, an impurity [50], was as low as 0.14 at%.

The powders were quantified for shape and size, in terms of shape factor ($4\pi A/P^2$, A: area; P: perimeter) and Feret diameter respectively. A shape factor of 0.8 ± 0.12 implies that the powders were nearly spherical (shape factor of 1 corresponds to a perfect sphere). The powder diameter was 61 ± 12 µm, i.e. in the range 40–90 µm. Both these measures suite the powders for laser synthesis [51–54]. Details on powder microstructure are provided in Supplementary Note 1.

2.2. Laser metal deposition (LMD)

The alloys were processed using a 5-axis handling system that was equipped with a fiber-coupled diode laser LDM 3000-60 (Laserline GmbH Mülheim-Kärlich, Germany). The laser wavelength was 976 nm. For the synthesis experiments, the laser power and laser beam diameter were 1.5 kW and 1.8 mm. The optimized hatch distance to achieve a dense sample was 800 µm. A uni-directional scan strategy was employed for deposition of layers. The thickness of each deposited layer was maintained at 200 µm. Four such layers were deposited on a substrate made of a copper alloy, Hovadur® K220 (Cu–2.4Ni–0.4Cr–0.7Si (wt%)). The synthesized sample height is nearly 1000 µm. Note that LMD belongs to the process category known as Directed Energy Deposition (DED) [55].

2.3. Microstructural characterization

The sample preparation for scanning electron microscopy (SEM) was performed using standard metallographic techniques. SEM was performed on a Zeiss Merlin system equipped with a field emission gun (FEG). For image acquisition, a voltage of 15 kV was maintained. The maximum probe current was 4 nA. Both these parameters also suited chemical compositional analysis by energy-dispersive X-ray spectroscopy (EDS). Elemental mappings by EDS

were performed with a Bruker Quantax system, and the results analyzed using an Esprit software version 2.1. Electron backscattered diffraction (EBSD) measurements were performed on a JEOL JSM-6500F microscope, using TSL OIM EBSD system, at an accelerating voltage of 15 kV.

2.4. High resolution characterization

Atom probe tomography (APT) was performed for a detailed chemical compositional analysis of in-situ formed Cr precipitates and of Laves phase particles. Material samples for APT were prepared by micro-machining with a focused ion beam (FIB). For this, a dual-beam FEI Helios 600 system was used. Measurement of Laves phase particle, in particular, required the sample preparation to be site-specific. The samples were prepared by annular milling until a specimen with an apex tip radius of less than 50 nm was reached [56]. The APT measurements were conducted on a LEAP 5000 XS system supplied by Cameca Instruments. The system was associated with a straight ion flight path and a detection efficiency of 80%. The specimens were measured in the laser pulsing mode. The laser pulse energy and the pulse repetition rate were 40 pJ and 200 kHz. The target detection rate was set to 5 ions per 2000 pulses on average (equivalent to 0.25%), and the base temperature maintained at 80 K. The acquired measured data were reconstructed and visualized using an IVAS® version 3.6.14 software.

Among reconstructed atoms, the Cr precipitate boundary was defined at 10 at% Cr using the Proximity Histogram Algorithm [57]. The sampling-volume-width was 0.5 nm. For determining the diameter and the number density of the Cr precipitates, the Maximum Separation Algorithm [58,59] based cluster analysis was performed.

For material characterization, at a larger length scale than that by APT, Transmission electron microscopy (TEM) was performed. A Phillips CM-20 instrument was used, operated at 200 kV. The TEM specimens, of less than 100 nm in thickness, were prepared by FIB micro-machining.

2.5. Nano- and micro-hardness testing

We assessed the spatial homogeneity of alloy hardening based on nano-hardness values obtained from nano-indentations. Nano-hardness tests were performed using a Hysitron TriboScope

950 nano-indenter system, equipped with a pyramidal diamond Berkovich indenter. Scanning probe microscopy (SPM) imaging was performed at indentation sites after measuring the load-displacement curves. Measurements were conducted in the load-controlled mode using a piezo-actuator, and the maximum constant load was 5000 μN . Three sets of 10×10 indentations were performed, with load-displacement data measured for each indentation. For the precise calculation of hardness and modulus from the load-displacement curves, the geometry of the indenter tip was calibrated using a quartz crystal as a standard reference.

Vickers hardness was also measured on the synthesized material with a diamond pyramidal indenter from LECO Instruments (AMH-43). The measurements were performed with a load of 50 gm. A minimum of 12 indents were placed on each sample.

2.6. Thermal conductivity

Thermal conductivity at room temperature was calculated using the Rosenthal's 3D heat conduction model for a point heat source [60,61]. The predicted temperature contour that corresponds to the alloy melting temperature was validated with the measured steady-state melt pool depth from SEM micrographs. The laser absorptivity was 0.08 [62], with a scattering multiplicity factor of 6 [63]. The multiplicity factor accounts for scattering due to spherical power geometry, as compared to flat surface geometry. The low alloying amount in the synthesized alloy was considered for approximating the temperature dependence of conductivity to be that for pure copper [64,65].

3. Microstructure characterization results

3.1. Dense sample fabrication and microstructure

Fig. 2(a) and (b) reveal the SEM-back scattered electron micrographs of the as-synthesized sample by LMD. These are taken along an orthogonal section to the laser scan direction (xz plane). In the as-built sample, the adjacent melt pools have overlapped. The pool boundaries, after solidification, are marked in red. Note that a hatch spacing distance maintained during LMD of 800 μm is lower than the melt pool width (~ 1 mm). This contributes to dense fabrication with low porosity. Porosity measured in the sample, using Image analysis of micrographs [66], is a mere 0.12%.

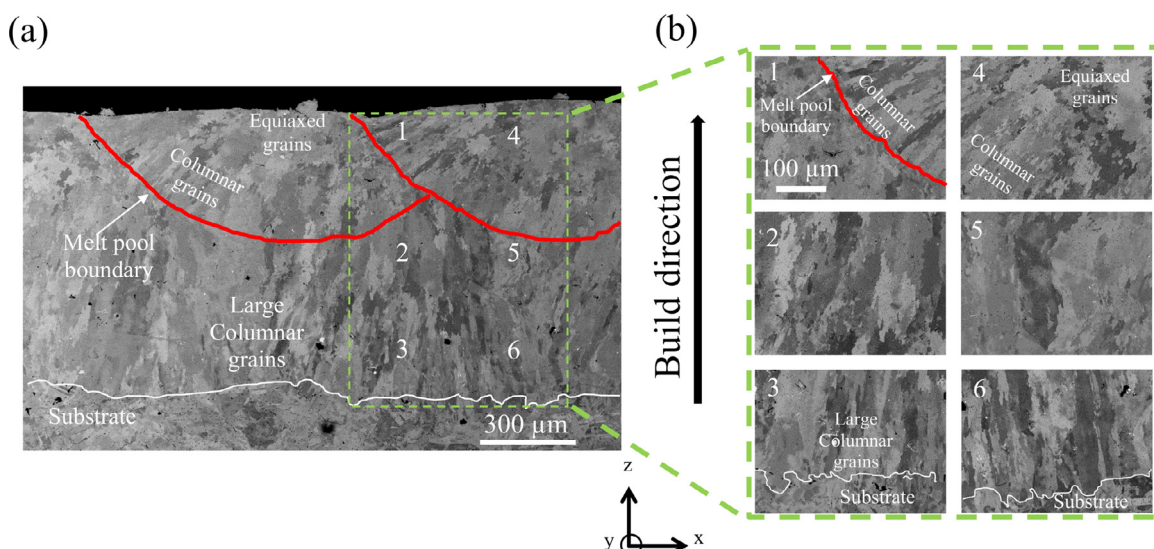


Fig. 2. (a) Backscattered SEM micrograph of the as-synthesized LMD microstructure taken along an orthogonal section to the laser scan direction. A low porosity (mean) of 0.12% is measured. (b) The magnified microstructure of the regions marked as 1–6 in (a).

Based on the low measured porosity, the as-built sample is considered to be a fully dense additive manufactured (AM) material ($< 0.5\%$ porosity) [46,67].

At the bottom of the built material adjoining the substrate, i.e. in the first deposited layers, large columnar grains constitute the microstructure (mean Feret diameter of $78\text{ }\mu\text{m}$). These directionally grown grains are nearly parallel to the build direction 'z'. The observation is typical of LMD produced microstructures [68–70]. Epitaxial growth favors the continuation of columnar grains in the subsequent layers (regions labeled 2–3, 5–6) except for the uppermost layer [71–73].

The last deposited layer along the build direction (marked in red) comprises both equiaxed and columnar grains (mean Feret diameters of $17\text{ }\mu\text{m}$ and $40\text{ }\mu\text{m}$ respectively). The regions are labeled as '1' and '4' in Fig. 2(a) and (b). The temperature gradient and solidification rate, which are location-dependent in the melt pool [41,74], dictate the grain morphologies.

The upper region of each deposited layer is expected to comprise equiaxed grains at a timeframe, before the deposition of a subsequent layer. The maintained layer height during synthesis ensures that the regions with equiaxed grains participate in remelting, as the subsequent layer gets deposited. This explains the grain structure in the re-melted locations in the lower layers, consisting of columnar grains (including those epitaxially grown), instead of equiaxed grains. The present synthesis does not negate the possibility of columnar grained microstructure until the uppermost layer, considering scaling up of the build size. The microstructure of the deposited layers below the uppermost layer, the region entirely containing large columnar grains, is referred to as the representative microstructure.

3.2. Laves phase micro-particles

SEM and EDS images in Fig. 3(a) and (b) indicate homogeneous distribution of particles in the microstructure. The particles

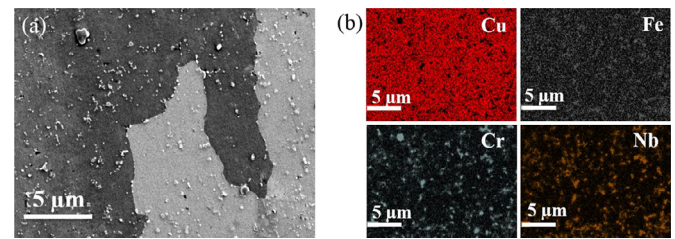


Fig. 3. (a) SEM micrograph taken from the representative microstructure (region 2 in Fig. 2) reveals a homogeneous distribution of Laves phase particles. (b) The EDS elemental mapping suggests that the particles are enriched in Cr, Nb and Fe.

are enriched in Cr, Nb and Fe. The volume fraction of the sub-micron sized particles, as determined by image analysis of SEM micrographs [75], is $2.2 \pm 0.1\%$. The maximum particle diameter is $1.1\text{ }\mu\text{m}$, which compares well with $1.2\text{ }\mu\text{m}$ for a Cu–8Cr–4Nb (at%) alloy processed conventionally in a previous study [35].

Fig. 4 shows chemical compositional analysis of a particle in the copper matrix by APT. Fig. 4(a) reveals APT reconstruction of the particle along the (002) crystallographic pole of the copper matrix. The pole identification is based on the observed symmetry on the detector for the FCC crystal structure [76–80]. The reconstructed inter-planar distance of the alloy matrix was calibrated with the (002) inter-planar distance in pure copper.

APT reconstructions show enrichment of Cr, Nb and Fe in the particles, corroborating the SEM-EDS mapping results. Fig. 4(b) displays chemical composition profile across the particle and into the matrix. The measured particle composition (mean) is 50 at% Cr, 12 at% Fe and 36 at% Nb. The stoichiometry corresponding to the measured composition matches the $(\text{Cr,Fe})_2\text{Nb}$ stoichiometry. The particle is inferred to be the Laves phase.

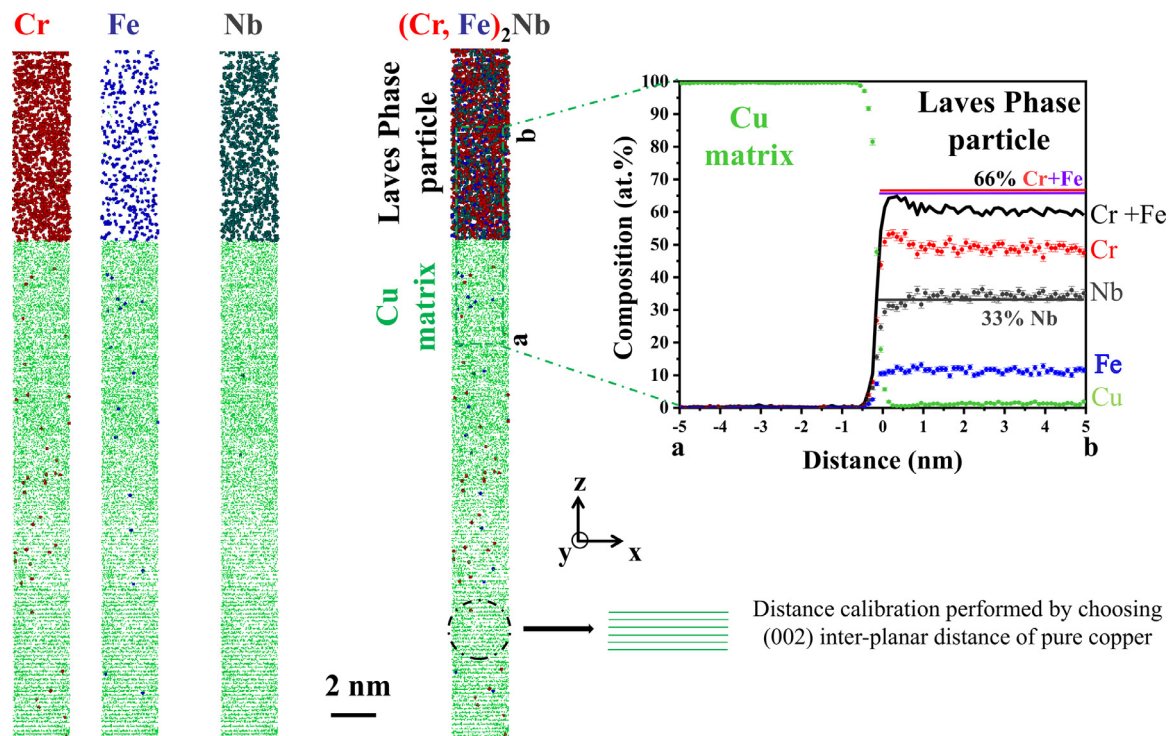


Fig. 4. (a) APT reconstruction of a Laves phase particle in the copper matrix. The (002) pole of the face-centered cubic (FCC) is identified for the copper matrix, based on the observed pole symmetry mapped by the detector. The (002) inter-planar distance in pure copper was used for distance calibration along the 'z'-direction, i.e. along the normal to the detector plate. (b) The plot of 1D chemical compositional profile across the Laves phase particle and into the matrix.

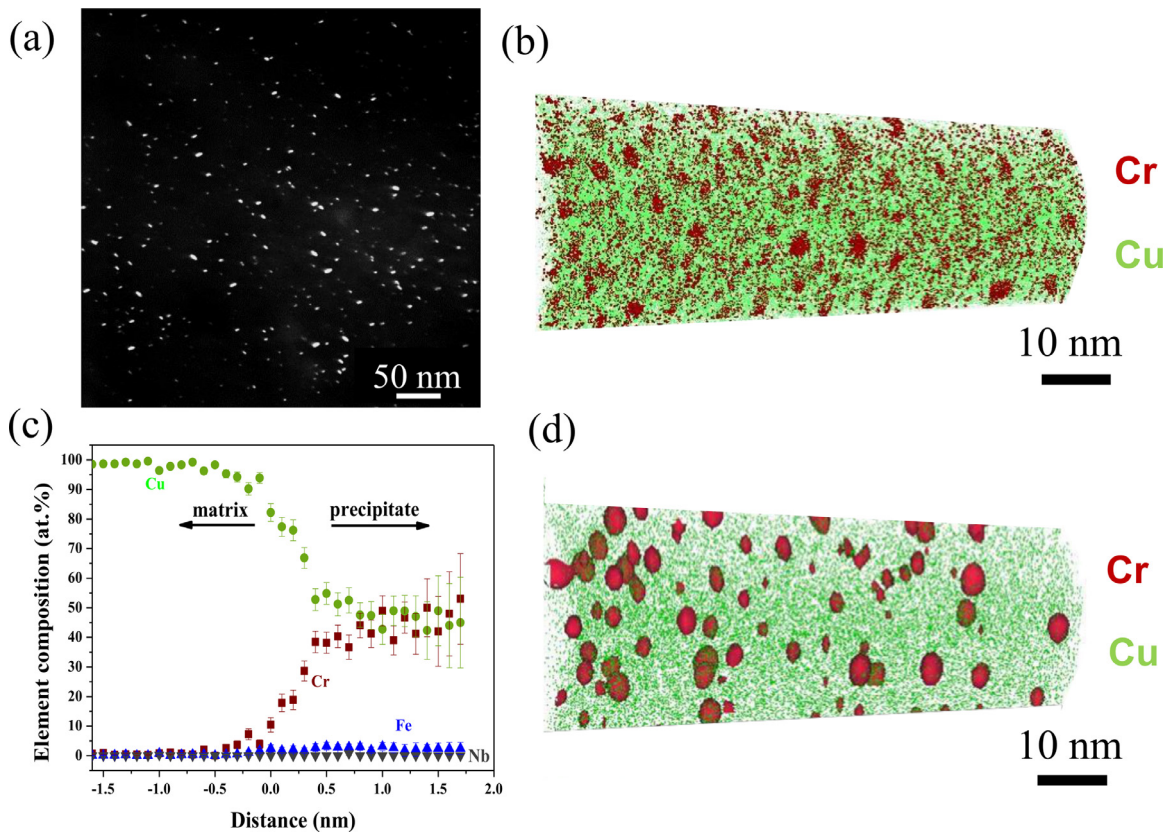


Fig. 5. (a) The TEM dark field image reveals a homogeneous distribution of nano-scale precipitates. (b) APT reconstruction reveals homogeneously distributed precipitates to contain Cr and to be 4 nm in diameter (mean). (c) Proximity histogram plot for 10 at% Cr iso-composition surfaces. Elemental composition plotted against the distance that is perpendicular to the precipitate-matrix interface. (d) The APT reconstruction displays precipitate interfaces corresponding to 10 at% Cr iso-composition surfaces.

3.3. Chromium nano-scale precipitates

Fig. 5(a) shows a dark field TEM image for a diffused (220) diffraction spot, acquired along the [111] zone axis of the copper matrix. Similar TEM studies performed earlier [81–84] revealed a homogeneous distribution of nm-sized coherent precipitates containing Cr. The APT reconstruction in Fig. 5(b) confirms an apparent homogeneous distribution of fine nano-scale precipitates. These are 4 ± 0.4 nm in diameter with a number density of $8 \times 10^{23} \text{ m}^{-3}$. The observation remains consistent across randomly sampled volumes in the representative microstructure of the synthesized alloy. The Cr precipitate interface definition follows the convention described by Chbihi et al. [50], which excludes one sampling-volume-thickness of the Cr gradient beginning from the copper matrix into the precipitate. Hence, we define the precipitate interface corresponding to 10 at% Cr, as shown in Fig. 5(d). Fig. 5(c) shows the proximity histogram for Cr precipitates for 10 at% iso-composition surfaces. The composition of the precipitate approaches an equiatomic amount (50 at%) of Cr and Cu.

4. Mechanical and thermal properties

4.1. Nano-hardness and elastic modulus determined from nano-indentation

Fig. 6(a) shows the nano-indentation sites. These are located in the representative microstructure of the LMD synthesized material that contains columnar grains. The indentation length scale is about 10 μm , i.e. the size of a nano-indent along with its surrounding strain field (cf. inset in Fig. 6(b)). The inter-indentation distance

for nearest neighbors was maintained at 40 μm . Fig. 6(b) shows the indentation load-displacement curve. The nano-hardness is determined from each curve using the established procedure by Oliver and Pharr [85].

Fig. 6(c) displays the comparison of nano-hardness for the present alloy against that for pure copper [86]. The comparison indicates substantial hardening in the present LMD-synthesized alloy. The nano-hardness (H) measures 2.12 ± 0.2 GPa. This is up to 2.5 times that of pure copper (conventionally processed and annealed) [86]. The standard deviation for the measured nano-hardness is 10% of the mean. Note that the standard deviation has a contribution from the crystallographic grain orientation anisotropy. In pure copper, the orientation anisotropy by itself leads to a standard deviation of 5% of the mean [86,87].

Fig. 6(d) presents a 2D contour plot for nano-hardness. The contour plot indicates that the nano-hardness values are spatially homogeneous in the representative microstructure (99% of the measured values lie within two standard deviations from the mean). Fig. 6(e) reveals the inverse pole figure (IPF) map, obtained from EBSD, at the nano-indentation sites (the region that corresponds to that in subfigure (d)). The measured nano-hardness does not hold a co-relation with the grain orientation of the alloy matrix.

The spatial homogeneity of hardening in the alloy is attributed to the homogeneous dual distribution of in-situ Cr precipitates and of Laves particles.

$$\frac{1}{E_r} = \frac{1 - \nu^2}{E} + \frac{1 - \nu_i^2}{E_i} \quad (1)$$

The elastic modulus, E , is calculated from the load-displacement curves using Eq. (1) [85]. The elastic modulus equates to 124 ± 9 GPa. In the equation, the reduced modulus, E_r , has been

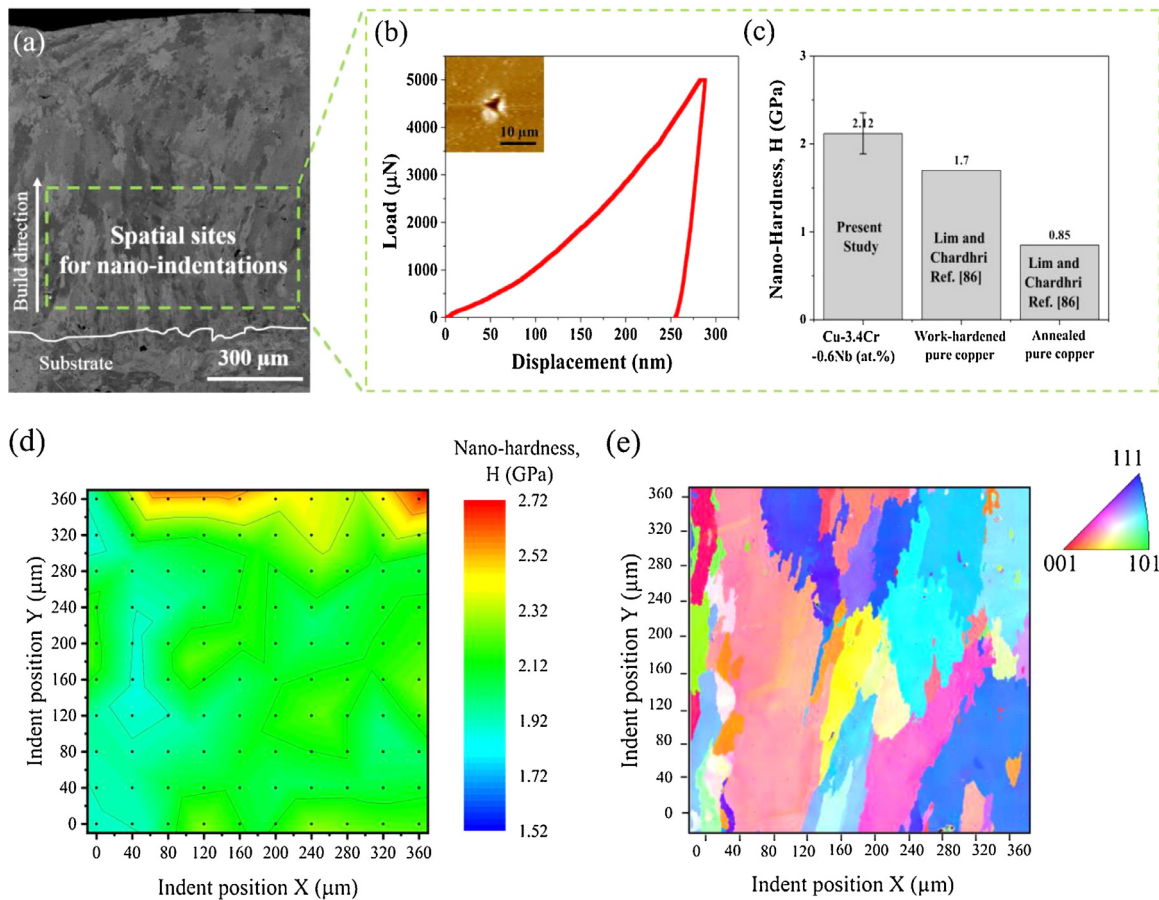


Fig. 6. (a) Nano-indentation sites in a representative portion of the LMD microstructure containing columnar grains. (b) Nano-indentation load-displacement curve; scanning probe microscopy image of a nano-indent in the inset. (c) Nano-hardness values of the present alloy compared with that of pure copper from Ref. [86]. (d) 2D spatial contour plot for visualization of the nano-hardness data implying spatial homogeneity of alloy hardening. Each indent position is represented by a black colored dot. (e) An inverse pole figure (IPF) map of the region which corresponds to that in (d).

determined experimentally and is 126 ± 8 GPa; with a Poisson's ratio, ν , of 0.35 [88]; the ' ν_i ' and ' E_i ' were 0.07 and 1141 GPa respectively (the subscript 'i' denotes the indenter). The calculated elastic modulus compares well with those values reported for Cu-8Cr-4Nb and Cu-4Cr-2Nb (at%) alloys, as these values approach 120 GPa [9].

Beyond the representative microstructural region, the homogeneity of hardening remains preserved, more specifically in the upper-most layer (comprising equiaxed grains). The nano-hardness is 2.36 ± 0.2 GPa, and the elastic modulus, 128 ± 8 GPa. The former is 11% higher than that corresponding to the lower layers belonging to the representative region.

4.2. Vickers hardness

Vickers hardness, which is a more spatially average measure of hardness compared to that by nano-indentation, is performed in the synthesized alloy. The plot in Fig. 7 compares the measured Vickers hardness with those for Cu-Cr-Nb ternary alloys studied previously. The alloying amount, i.e. Cr and Nb (at%), is plotted in the same graph. The present alloy hardness is 146 ± 13 HV. This is about three times high than that reported for pure copper of 50 HV [9].

In a conventionally processed (as-extruded) Cu-4Cr-2Nb (at%) alloy [9], a hardness of 117 HV was reported. In Cu-8Cr-4Nb (at%) alloys, which contain higher alloying amount than that in Cu-4Cr-2Nb (at%), the hardness values were shown to reach 128–132 HV [9,35]. These previous studies have indicated that a hardness in-

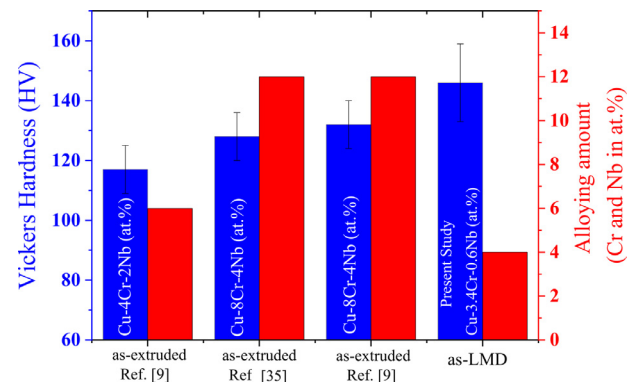


Fig. 7. The Vickers hardness plot compares the presently synthesized alloy with Cu-Cr-Nb reference alloys reported previously [9,35]. The alloying amount, of Cr and Nb (at%), is also plotted in the same graph.

crease requires a greater alloying amount (an increase from 6 at% in Cu-4Cr-2Nb to 12 at% in Cu-8Cr-4Nb). We have achieved the hardening effect in the present alloy with a mere 4 at% alloying amount.

4.3. Thermal conductivity

The room temperature thermal conductivity of the synthesized alloy evaluates to 68% IACS. In previously studied Cu-4Cr-2Nb

(at%) and Cu–8Cr–4Nb (at%) alloys, processed conventionally, the reported conductivity values were 74% and 54% IACS respectively [9].

5. Discussion

5.1. Effect of secondary phases on alloy hardening

In conventionally produced Cu–8Cr–4Nb (at%) and Cu–4Cr–2Nb (at%) systems, studied previously, alloy hardening has relied upon Laves phase particles of Cr₂Nb. More specifically, the hardening in these materials was attributed to a direct contribution from such second phase dispersed particles constituting 7–14 vol% [9,35,49]. Additionally, an indirect hardening contribution from these particles was because of the Hall–Petch effect, i.e. due to particle-induced grain refinement (grain diameter $\sim 2.7 \mu\text{m}$) [9,35,49]. Each of these particle hardening contributions are expected to be less dominant in the present alloy; the present microstructure constitutes a mere 2.2 vol% of comparable sub-micron sized Laves phase particles and coarse grains of 78 μm in diameter (mean).

In the present alloy, however, the coherency hardening contribution due to the in-situ Cr precipitation is a substantial 234 MPa (78 HV as converted by Tabor's approximation [89]). This calculated contribution assumes a lattice misfit mechanism (further details in Supplementary note: 2), considering the precipitates to be of FCC crystal structure [50].

The hardening contribution from the sub-micron sized Laves phase particles is 22 HV, according to the Orowan–Ashby relation for incoherent particles [9,90] (details in Supplementary note: 2). The two individual contributions, i.e. from in-situ Cr precipitates and Laves particles, along with the base hardness of pure copper (50 HV [9]) add to 150 HV. This corresponds well with the measured hardness of 146 HV.

The measured hardness can reach values as high as those reported for lean ternary Cu–Cr–Ag [29] and Cu–Cr–Zr [23,50] alloys. For example, Cu–0.3Cr–0.1Ag (wt%) alloy hardness in a peak-aged state was shown to be 144 HV [29]. In a Cu–1Cr–0.1Zr (wt%) alloy, a peak-aged hardness of 155 HV was reported [50]. It must be noted that these quoted hardness values [29,50,91] were determined after an aging heat treatment following plastic straining. The hardness of the present alloy, however, is probed in the as-synthesized state without any subsequent heat treatment.

5.2. Effect of secondary phases on conductivity

The thermal conductivity values for Cu–4Cr–2Nb (at%) and Cu–8Cr–4Nb (at%) were reported in earlier work to be 74% and 54% IACS respectively [9]. The depreciation in conductivity values with Laves phase amount (from 7 to 14 vol%) has been attributed to interfacial inelastic electron scattering.

Interfacial scattering in the current material is not only from the Laves phase particles but also from the in-situ formed Cr precipitates. Despite both scattering contributions, a conductivity of 68% IACS can be reached in the present alloy. The Laves phase particles, whose sizes are comparable to those reported in Ref. [9], constitute a mere 2.2 vol%. Their interfacial scattering, according to the behavior in Ref. [9], would account for conductivity depreciation (with reference to pure copper) of about 14% IACS. Likewise, Cr precipitate contribution to scattering would be equivalent to a 24% IACS depreciation [50]. Note that the latter also accounts for the scattering also due to Fe impurity [50,92]. In the synthesized alloy, Fe impurity partitions to the Laves particles, as it leaves the copper matrix. These particles, dispersed across the microstructure, sequester [93,94] the Fe impurities. The observed conductivity of 68% IACS in the designed alloy is thus explained by considering the individual scattering contributions.

Collective property evaluation of hardness (HV) and conductivity (k) (based on the metric HV^{*}k from Ref. [9]), suggests a range starting from 350 (GPa W/mK) in prior Cu–Cr–Nb ternary alloys. The present alloy corresponds to 390 (GPa W/mK). The alloying amount, Cr and Nb (at%), to design the current alloy for in-situ LMD processing, is justified.

5.3. In-situ chromium precipitation kinetics during laser metal deposition (LMD)

In-situ Cr precipitation leads to a substantial hardening effect. Kinetics of the Cr precipitation for hardening is decisively dependent on chromium alloying amount (in the range of up to 5 at%), and on cooling rate during processing (in the range of 10^2 – 10^6 K/s).

LMD, a solidification processing route, leads to a cooling rate of 10^3 – 10^4 K/s [95]. Solidification processing route by casting (cooling rate $< 10^2$ K/s) has been explored, in the binary Cu–Cr lean system. The casting route does not achieve Cr precipitation hardening because of incoherent Cr precipitates exceeding 1 μm in diameter [96,97].

Rapid solidification processing (RSP) route, which imposes a high cooling rate ($\sim 10^6$ K/s), results in a supersaturated solid solution of copper that contains dissolved Cr. This was shown in a Cu–2Cr (wt%) alloy microstructure [28]. The microstructure also contains 50 nm sized incoherent Cr primary precipitates (pro-eutectic) [28], in a Cu–5Cr (wt%) binary alloy (hypereutectic Cr amount). The hardening contribution from primary precipitates would be negligible (12 MPa or 4HV as predicted by Orowan–Ashby relation [9]). Note that the primary precipitates can at best be restricted to a 50 nm size, i.e. belongs to incoherent size regime, even upon imposing a high cooling rate of 10^6 K/s [28] that is higher than the cooling rate during LMD. Furthermore, a manifestation of Cr in solid solution also does not contribute to hardening in the binary Cu–Cr alloys [98,99].

The present alloy behaves as a quasi-binary Cu–Cr system, in the context of Cr precipitation. This is because Nb is contained entirely in the Laves phase particles, those that are not soluble in copper up to its melting temperature [100]. After alloy solidification progresses during LMD synthesis, to ensure sufficient Cr is available for precipitation, its alloying amount must be higher than that consumed in the Laves phase particles. About 1.6 at% Cr is made available for precipitation, as 3.4 at% Cr is the total amount in the alloy. Note that the available alloying amount approaches the eutectic amount in binary Cu–Cr system [101].

If the effective chromium alloying amount for precipitation were to be significantly increased above the eutectic amount, i.e. in the hyper-eutectic compositional regime, then primary incoherent Cr precipitates during LMD synthesis is expected. These precipitates cannot be fine enough to belong to the coherent size regime of less than 10 nm [28,30], as the cooling rate in LMD is not as high as that in RSP.

The presently observed hardening effect from the Cr precipitates (4 nm mean diameter) is substantial, as these belong to the coherent size regime in copper alloys [28]. By identifying a suited combination of in-process cooling rate and chromium alloying amount, we have exploited Cr precipitation hardening. Fig. 8(a) shows a schematic plot that compares as-processed microstructures, by solidification routes in Cu–Cr lean alloys, as a function of chromium alloying amount (at%) available for precipitation and cooling rates during processing. The solidification processing routes displayed are for casting [96,97], RSP [28] and LMD. The Cu–Cr binary phase diagram in the vicinity of the eutectic composition [101], is shown in subfigure (b).

In-situ microstructural tailoring during laser additive manufacturing [102,103], to achieve precipitation has been reported earlier.

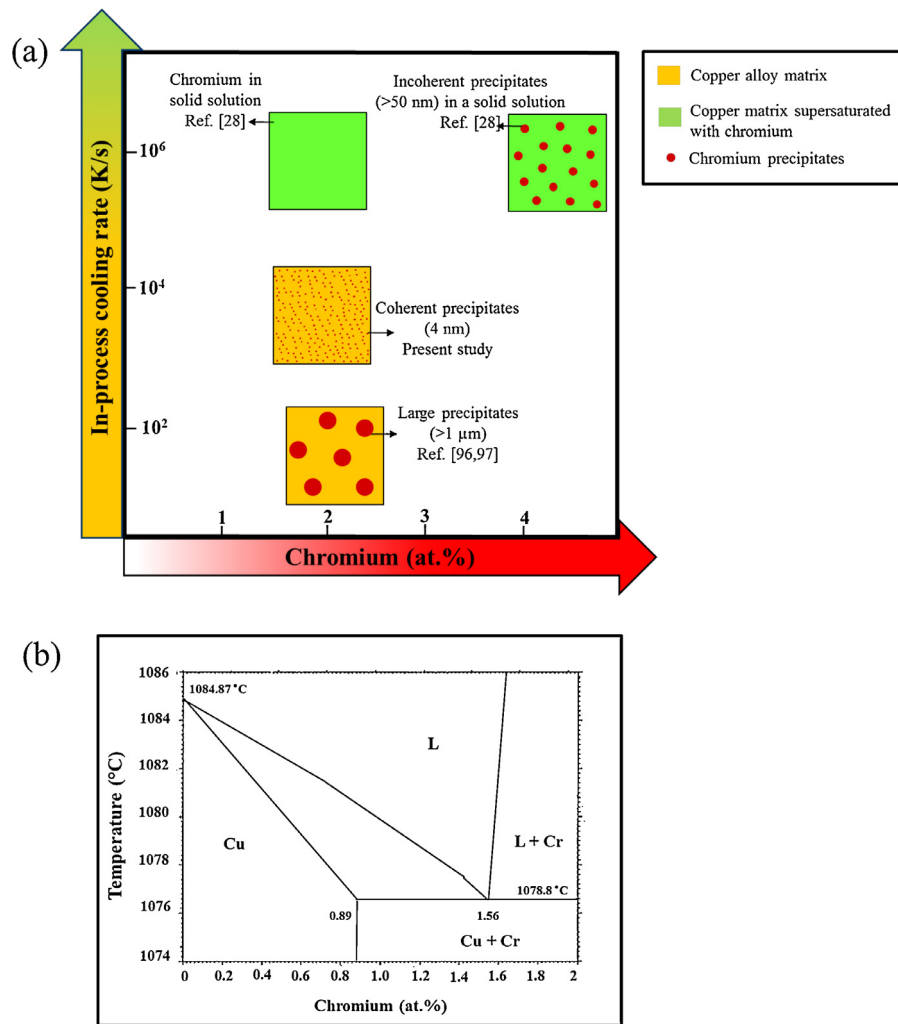


Fig. 8. (a) Schematic plot comparing solidification microstructures between the present Cu–Cr quasi-binary alloy processed by LMD against those in lean binary Cu–Cr alloys studied earlier by casting and by rapid solidification processing [28,96,97]. The chromium amount (at%) in the alloy available for precipitation and the in-process cooling rate (K/s) are represented along the abscissa and the ordinate respectively. For alloy hardening via Cr precipitation, we have identified an optimal chromium alloying amount that suits the inherent LMD cooling rate. (b) The Cu–Cr binary phase diagram in the vicinity of the eutectic composition as reproduced from [101].

More specifically, exploiting of the intrinsic heat treatment (IHT) effect for precipitation hardening has been shown in ferrous materials like maraging steels [45] and in aluminum based alloys [104]. IHT has an analogous effect as an aging heat treatment, due to an accompanying temperature pulse with each deposited layer. If the IHT effect were to be dominant in the present alloy, then a hardness gradation with build height must have been observed.

Here, we have shown in-situ Cr precipitation even with no dominance of IHT, as the measured hardness profiles are spatially homogeneous. The behavior can be attributed to a high thermal conductivity associated with the synthesized microstructure, permitting rapid heat dissipation, away from each deposited layer. A low material thermal conductivity, of the material while being built, could have markedly undermined coherency strengthening contribution because of coarsened Cr precipitates; this undesired outcome is particularly possible in an alloy in the Cu–Cr based system with a narrow coherent precipitate size regime of up to a mere 10 nm [28,30]. Note that heat conduction is the primary heat removal mechanism in additively manufactured alloys [45].

The suppression of precipitate coarsening is contingent also upon the choice of substrate material, one that prevents heat accumulation in the deposited alloy. This rationale has governed the selection of a lean K220 copper alloy as the substrate material for the

present synthesis, based on the similarity of thermal diffusivity between the substrate and the deposited alloy (additional details in the supplementary note: 3). Besides, with this choice, the probability is low for the formation of undesired intermetallic compounds at the interface with the deposited alloy.

The deposited alloy surface, particularly the upper-most layer, has 11% higher hardness than that of the bulk. The surface hardening effect is beneficial in copper alloys due to enhanced wear resistance [105]. This effect is an added benefit of the synthesis approach.

Considering the scaling-up of the build size to tens or hundreds of mm via deposition based additive manufacturing, the possibility of precipitate coarsening could still be negated. For this purpose, a broader deposition process variable space that also contains pause duration between layers, and substrate cooling imposed with additional apparatus, may be explored during synthesis.

In summary, the current work illustrates an in-situ synthesis approach by LMD in a lean Cu–3.4Cr–0.6Nb (at%) alloy. A combination of high strength and conductivity is associated with the synthesized material. For achieving the property combination, we have shown that any heat treatment step post-synthesis is not necessary. Such a step was previously inevitable for processing lean Cu–Cr based alloys, particularly by routes involving solidification.

6. Conclusions

- 1 We have demonstrated an in-situ laser metal deposition (LMD) based synthesis approach to produce a conductive and strong Cu–Cr–Nb alloy. A post-process heat treatment step, which had been previously indispensable to processing of lean Cu–Cr based systems, has been obviated. The synthesized material has a Vickers hardness of 146 and a thermal conductivity of 68% IACS, at room temperature.
- 2 The as-synthesized alloy microstructure contains in-situ formed nano-scale Cr precipitates (4 nm diameter; number density $8 \times 10^{23} \text{ m}^{-3}$). These are distributed homogeneously in a nearly pure copper matrix. Laves phase sub-micron particles are also dispersed in the microstructure, whose amount has been relied upon previously for hardening Cu–Cr–Nb alloys, and is present in an amount as low as 2.2 vol%.
- 3 For substantial hardening from in-situ Cr precipitation, we have designed the Cu–Cr quasi-binary alloy. Nb is contained entirely in the Laves phase particles, those that are insoluble in the copper matrix, apart from some Cr in them. We have conceived an additional Cr alloying amount ($\sim 1.6 \text{ at\%}$) available for precipitation, i.e. it approaches the binary Cu–Cr eutectic composition. Further chromium alloying amount is expected to result in pro-eutectic Cr precipitation that does not contribute to hardening.
- 4 The cooling rate during LMD (10^3 – 10^4 K/s [95]) leads to a Cr precipitate size that belongs to the coherent regime, resulting in substantial hardening. A departure from this optimal cooling rate does not realize such an extent of hardening; a high cooling rate of 10^6 K/s leads to Cr supersaturation in the solid solution [28], whereas a low cooling rate of 10^2 K/s leads to large Cr particles ($> 1 \mu\text{m}$) [96,97].

By identifying the desired combination of in-process LMD cooling rate and chromium alloying amount, we have demonstrated an in-situ synthesis approach to achieve a microstructure associated with high strength along with conductivity. The work presents a novel solidification processing avenue via beam-based additive manufacturing, advancing alloy development in the Cu–Cr–Nb ternary space.

Declaration of Competing interest

The authors declare that they have no known competing financial interests or personal relationships that could have appeared to influence the work reported in this paper.

Acknowledgments

The current research work has been carried out with the financial support from the AProLAM project, funded by the strategic collaboration between the Fraunhofer Society and the Max Planck Society. The authors are grateful for the technical support extended by Mr. Uwe Tezins and Mr. Andreas Sturm for the atom probe tomography and the focused ion beam facilities at the Max-Planck-Institut für Eisenforschung. The authors also acknowledge Ms. Monika Nellesen and Ms. Katja Angenendt for the support with scanning electron microscopes. The authors express gratitude to Ms. Heidi Bögershausen in connection with nano-indentation and hardness measurements.

Supplementary materials

Supplementary material associated with this article can be found, in the online version, at doi:[10.1016/j.actamat.2020.07.035](https://doi.org/10.1016/j.actamat.2020.07.035).

References

- [1] D. Raabe, D. Mattissen, Microstructure and mechanical properties of a cast and wire-drawn ternary Cu–Ag–Nb in situ composite, *Acta Mater.* 46 (1998) 5973–5984, doi:[10.1016/S1359-6454\(98\)00218-3](https://doi.org/10.1016/S1359-6454(98)00218-3).
- [2] Y. Sakai, K. Inoue, T. Asano, H. Maeda, Development of a high strength, high conductivity copper-silver alloy for pulsed magnets, *IEEE Trans. Magn.* 28 (1992) 888–891, doi:[10.1109/20.120021](https://doi.org/10.1109/20.120021).
- [3] D. Raabe, S. Ohsaki, K. Hono, Mechanical alloying and amorphization in Cu–Nb–Ag in situ composite wires studied by transmission electron microscopy and atom probe tomography, *Acta Mater.* 57 (2009) 5254–5263, doi:[10.1016/j.actamat.2009.07.028](https://doi.org/10.1016/j.actamat.2009.07.028).
- [4] J.D. Embury, M.A. Hill, W.A. Spitzig, Y. Sakai, Microstructural aspects of materials for nondestructive long-pulse high-field magnets, *MRS Bull.* 18 (1993) 57–60, doi:[10.1557/S0883769400037799](https://doi.org/10.1557/S0883769400037799).
- [5] Y. Sakai, K. Inoue, H. Maeda, High-strength and high-conductivity Cu–Ag alloy sheets: new promising conductor for high-field Bitter coils, *IEEE Trans. Magn.* 30 (1994) 2114–2117, doi:[10.1109/20.305687](https://doi.org/10.1109/20.305687).
- [6] D. Raabe, K. Miyake, H. Takahara, Processing, microstructure, and properties of ternary high-strength Cu–Cr–Ag in situ composites, *Mater. Sci. Eng. A* 291 (2000) 186–197, doi:[10.1016/S0921-5093\(00\)00981-3](https://doi.org/10.1016/S0921-5093(00)00981-3).
- [7] P. Jain, S.V. Raj, K.J. Hemker, Characterization of NiCrAlY coatings for a high strength, high conductivity GRCo-84 copper alloy, *Acta Mater.* 55 (2007) 5103–5113, doi:[10.1016/j.actamat.2007.05.044](https://doi.org/10.1016/j.actamat.2007.05.044).
- [8] S.V. Raj, L.J. Ghosn, C. Robinson, D. Humphrey, High heat flux exposures of coated GRCo-84 substrates, *Mater. Sci. Eng. A* 457 (2007) 300–312, doi:[10.1016/j.msea.2006.12.133](https://doi.org/10.1016/j.msea.2006.12.133).
- [9] K.R. Anderson, J.R. Groza, Microstructural size effects in high-strength high-conductivity Cu–Cr–Nb alloys, *Metall. Mater. Trans. A* 32 (2001) 1211–1224, doi:[10.1007/s11661-001-0130-x](https://doi.org/10.1007/s11661-001-0130-x).
- [10] D. Raabe, J. Ge, Experimental study on the thermal stability of Cr filaments in a Cu–Cr–Ag in situ composite, *Scr. Mater.* 51 (2004) 915–920, doi:[10.1016/j.scriptamat.2004.06.016](https://doi.org/10.1016/j.scriptamat.2004.06.016).
- [11] ASM Handbook Volume 2, Properties and Selection: Nonferrous Alloys and Special-Purpose Materials, ASM International, 2017 http://www.asminternational.org/home/-/journal_content/56/10192/06182C/PUBLICATION/ accessed September 20.
- [12] Resources: Standards & Properties – Copper & Copper Alloy Microstructures: Chromium Copper, https://www.copper.org/resources/properties/microstructure/chrom_cu.html (accessed December 18, 2017).
- [13] A.O. Olofinjana, A. Atrens, Properties of rapidly solidified binary copper alloys, *Mater. Lett.* 31 (1997) 87–92, doi:[10.1016/S0167-577X\(96\)00253-4](https://doi.org/10.1016/S0167-577X(96)00253-4).
- [14] D.L.M. Ellis, Precipitation Strengthened High Strength, High Conductivity Cu–Cr–Nb Alloys Produced by Chill Block Melt Spinning. Final Report Ph.D. Thesis, 1989. <https://ntrs.nasa.gov/search.jsp?R=19900002537> (accessed November 10, 2017).
- [15] P.M. Berge, S.T. Kim, E.D. Gibson, J.D. Verhoeven, An air melting technique for preparing Cu–Cr alloys, *JOM* 50 (1998) 42–43, doi:[10.1007/s11837-998-0193-x](https://doi.org/10.1007/s11837-998-0193-x).
- [16] W.A. Soffa, D.E. Laughlin, High-strength age hardening copper–titanium alloys: redivivus, *Prog. Mater. Sci.* 49 (2004) 347–366, doi:[10.1016/S0079-6425\(03\)00029-X](https://doi.org/10.1016/S0079-6425(03)00029-X).
- [17] R.D.K. Misra, V.S. Prasad, P.R. Rao, Dynamic embrittlement in an age-hardenable copper–chromium alloy, *Scr. Mater.* 35 (1996) 129–133, doi:[10.1016/1359-6462\(96\)00098-X](https://doi.org/10.1016/1359-6462(96)00098-X).
- [18] V.A. Phillips, Electron microscope observations on precipitation in a Cu–1.07% Zr alloy, *Metallography* 7 (1974) 137–155, doi:[10.1016/0026-0800\(74\)90003-2](https://doi.org/10.1016/0026-0800(74)90003-2).
- [19] M. Kapoor, T. Kaub, K.A. Darling, B.L. Boyce, G.B. Thompson, An atom probe study on Nb solute partitioning and nanocrystalline grain stabilization in mechanically alloyed Cu–Nb, *Acta Mater.* 126 (2017) 564–575, doi:[10.1016/j.actamat.2016.12.057](https://doi.org/10.1016/j.actamat.2016.12.057).
- [20] D.-P. Lu, J. Wang, W.-J. Zeng, Y. Liu, L. Lu, B.-D. Sun, Study on high-strength and high-conductivity Cu–Fe–P alloys, *Mater. Sci. Eng. A* 421 (2006) 254–259, doi:[10.1016/j.msea.2006.01.068](https://doi.org/10.1016/j.msea.2006.01.068).
- [21] A. Vinogradov, V. Patlan, Y. Suzuki, K. Kitagawa, V.I. Kopylov, Structure and properties of ultra-fine grain Cu–Cr–Zr alloy produced by equal-channel angular pressing, *Acta Mater.* 50 (2002) 1639–1651, doi:[10.1016/S1359-6454\(01\)00437-2](https://doi.org/10.1016/S1359-6454(01)00437-2).
- [22] H. Wei, Y. Cui, H. Cui, Y. Wei, L. Hou, Effects of multiple trace alloying elements on the microstructure and properties of Cu–4wt% Ti alloys, *Mater. Sci. Eng. A* 707 (2017) 392–398, doi:[10.1016/j.msea.2017.09.072](https://doi.org/10.1016/j.msea.2017.09.072).
- [23] I.S. Batra, G.K. Dey, U.D. Kulkarni, S. Banerjee, Microstructure and properties of a Cu–Cr–Zr alloy, *J. Nucl. Mater.* 299 (2001) 91–100, doi:[10.1016/S0022-3115\(01\)00691-2](https://doi.org/10.1016/S0022-3115(01)00691-2).
- [24] L. Lu, Y. Shen, X. Chen, L. Qian, K. Lu, Ultrahigh strength and high electrical conductivity in copper, *Science* 304 (2004) 422–426, doi:[10.1126/science.1092905](https://doi.org/10.1126/science.1092905).
- [25] Y. Zhao, T.A. Furnish, M.E. Kassner, A.M. Hodge, Thermal stability of highly nanotwinned copper: the role of grain boundaries and texture, *J. Mater. Res.* 27 (2012) 3049–3057, doi:[10.1557/jmr.2012.376](https://doi.org/10.1557/jmr.2012.376).
- [26] C.-M. Liu, H.-W. Lin, Y.-S. Huang, Y.-C. Chu, C. Chen, D.-R. Lyu, K.-N. Chen, K.-N. Tu, Low-temperature direct copper-to-copper bonding enabled by creep on (111) surfaces of nanotwinned Cu, *Sci. Rep.* 5 (2015), doi:[10.1038/srep09734](https://doi.org/10.1038/srep09734).

- [27] L. Guillet, *Rev. Metall.* 3 (1906) 176.
- [28] M.A. Morris, D.G. Morris, Microstructures and mechanical properties of rapidly solidified Cu-Cr alloys, *Acta Metall.* 35 (1987) 2511–2522, doi:10.1016/0001-6160(87)90148-9.
- [29] S.G. Jia, M.S. Zheng, P. Liu, F.Z. Ren, B.H. Tian, G.S. Zhou, H.F. Lou, Aging properties studies in a Cu–Ag–Cr Alloy, *Mater. Sci. Eng. A* 419 (2006) 8–11, doi:10.1016/j.msea.2005.09.118.
- [30] J.B. Correia, H.A. Davies, C.M. Sellars, Strengthening in rapidly solidified age hardened Cu–Cr and Cu–Cr–Zr alloys, *Acta Mater.* 45 (1997) 177–190, doi:10.1016/S1359-6454(96)00142-5.
- [31] Q. Liu, X. Zhang, Y. Ge, J. Wang, J.-Z. Cui, Effect of processing and heat treatment on behavior of Cu–Cr–Zr alloys to railway contact wire, *Metall. Mater. Trans. A* 37 (2006) 3233–3238, doi:10.1007/BF02586158.
- [32] D.L. Ellis, GRCop-84: A High-Temperature Copper Alloy for High-Heat-Flux Applications, 2005. <https://ntrs.nasa.gov/search.jsp?R=20050123582> (accessed November 10, 2017).
- [33] H. Fu, S. Xu, W. Li, J. Xie, H. Zhao, Z. Pan, Effect of rolling and aging processes on microstructure and properties of Cu–Cr–Zr alloy, *Mater. Sci. Eng. A* 700 (2017) 107–115, doi:10.1016/j.msea.2017.05.114.
- [34] S.I. Hong, M.A. Hill, Microstructural stability and mechanical response of Cu–Ag microcomposite wires, *Acta Mater.* 46 (1998) 4111–4122, doi:10.1016/S1359-6454(98)00106-2.
- [35] K.R. Anderson, J.R. Groza, R.L. Dreshfield, D. Ellis, High-Performance dispersion-strengthened Cu–8 Cr–4 Nb alloy, *Metall. Mater. Trans. A* 26 (1995) 2197–2206, doi:10.1007/BF02671235.
- [36] D.L. Ellis, G.M. Michal, Formation of Cr and Cr₂Nb precipitates in rapidly solidified Cu–Cr–Nb ribbon, *Ultramicroscopy* 30 (1989) 210–216, doi:10.1016/0304-3991(89)90189-7.
- [37] V. Alekseenko, A. Alekseenko, The abundances of chemical elements in urban soils, *J. Geochem. Explor.* 147 (2014) 245–249, doi:10.1016/j.gca.2014.08.003.
- [38] E. Martinez, L.E. Murr, J. Hernandez, X. Pan, K. Amato, P. Frigola, C. Terrazas, S. Gaytan, E. Rodriguez, F. Medina, R.B. Wicker, Microstructures of niobium components fabricated by electron beam melting, *Metallogr. Microstruct. Anal.* 2 (2013) 183–189, doi:10.1007/s13632-013-0073-9.
- [39] Y. Guo, L. Jia, S. Sun, B. Kong, J. Liu, H. Zhang, Rapid fabrication of Nb–Si based alloy by selective laser melting: microstructure, hardness and initial oxidation behavior, *Mater. Des.* 109 (2016) 37–46, doi:10.1016/j.matdes.2016.07.048.
- [40] W.J. Sames, F.A. List, S. Pannala, R.R. Dehoff, S.S. Babu, The metallurgy and processing science of metal additive manufacturing, *Int. Mater. Rev.* 61 (2016) 315–360, doi:10.1080/09506608.2015.1116649.
- [41] C.L.A. Leung, S. Marussi, R.C. Atwood, M. Towrie, P.J. Withers, P.D. Lee, In situ X-ray imaging of defect and molten pool dynamics in laser additive manufacturing, *Nat. Commun.* 9 (2018) 1355, doi:10.1038/s41467-018-03734-7.
- [42] N.J. Harrison, I. Todd, K. Mumtaz, Reduction of micro-cracking in nickel superalloys processed by selective laser melting: a fundamental alloy design approach, *Acta Mater.* 94 (2015) 59–68, doi:10.1016/j.actamat.2015.04.035.
- [43] S. Tammas-Williams, I. Todd, Design for additive manufacturing with site-specific properties in metals and alloys, *Scr. Mater.* 135 (2017) 105–110, doi:10.1016/j.scriptamat.2016.10.030.
- [44] B. Vrancken, L. Thijs, J.-P. Kruth, J. Van Humbeeck, Microstructure and mechanical properties of a novel β titanium metallic composite by selective laser melting, *Acta Mater.* 68 (2014) 150–158, doi:10.1016/j.actamat.2014.01.018.
- [45] P. Kürnsteiner, M.B. Wilms, A. Weisheit, P. Barriobero-Vila, E.A. Jäggle, D. Raabe, Massive nanoprecipitation in an Fe–19Ni–xAl maraging steel triggered by the intrinsic heat treatment during laser metal deposition, *Acta Mater.* 129 (2017) 52–60, doi:10.1016/j.actamat.2017.02.069.
- [46] D. Herzog, V. Seyda, E. Wycisk, C. Emmelmann, Additive manufacturing of metals, *Acta Mater.* 117 (2016) 371–392, doi:10.1016/j.actamat.2016.07.019.
- [47] J. Harbaugh, NASA 3-D Prints First Full-Scale Copper Rocket Engine Part, NASA, 2015 <http://www.nasa.gov/marshall/news/nasa-3-d-prints-first-full-scale-copper-rocket-engine-part.html> accessed November 10, 2017.
- [48] P.R.P. Gradl, Progress in Additively Manufactured Copper-Alloy GRCop-84, GRCop-42, and Bimetallic Combustion Chambers for Liquid Rocket Engines, Washington, DC, United States, 2019, <https://ntrs.nasa.gov/search.jsp?R=20190033311> (accessed January 25, 2020).
- [49] K.R. Anderson, J.R. Groza, D.G. Ulmer, Microstructural refinement and strengthening of Cu–4 Cr–2 Nb alloy by mechanical milling, *Scr. Mater.* 37 (1997) 179–185, doi:10.1016/S1359-6462(97)00075-4.
- [50] A. Chbihi, X. Sauvage, D. Blavette, Atomic scale investigation of Cr precipitation in copper, *Acta Mater.* 60 (2012) 4575–4585, doi:10.1016/j.actamat.2012.01.038.
- [51] A.J. Pinkerton, An analytical model of beam attenuation and powder heating during coaxial laser direct metal deposition, *J. Phys. Appl. Phys.* 40 (2007) 7323, doi:10.1088/0022-3727/40/23/012.
- [52] D. Boisselier, S. Sankar, Influence of powder characteristics in laser direct metal deposition of SS316L for metallic parts manufacturing, *Phys. Proc.* 39 (2012) 455–463, doi:10.1016/j.phpro.2012.10.061.
- [53] H.J. Niu, I.T.H. Chang, Selective laser sintering of gas and water atomized high speed steel powders, *Scr. Mater.* 41 (1999) 25–30, doi:10.1016/S1359-6462(99)00089-5.
- [54] J. Dawes, R. Bowerman, R. Trepleton, Introduction to the additive manufacturing powder metallurgy supply chain, *Johns. Matthey Technol. Rev.* 59 (2015) 243–256, doi:10.1595/205651315X688686.
- [55] T. DebRoy, H.L. Wei, J.S. Zuback, T. Mukherjee, J.W. Elmer, J.O. Milewski, A.M. Beese, A. Wilson-Heid, A. De, W. Zhang, Additive manufacturing of metallic components – process, structure and properties, *Prog. Mater. Sci.* 92 (2018) 112–224, doi:10.1016/j.pmatsci.2017.10.001.
- [56] D.J. Larson, T.J. Prosa, R.M. Ulfing, B.P. Geiser, T.F. Kelly, Local Electrode Atom Probe Tomography: A User's Guide, Springer-Verlag, New York, 2013 www.springer.com/de/book/9781461487203 accessed March 31, 2018.
- [57] O.C. Hellman, J.A. Vandenbroucke, J. Rüsing, D. Isheim, D.N. Seidman, Analysis of three-dimensional atom-probe data by the proximity histogram, *Microsc. Microanal.* 6 (2000) 437–444, doi:10.1007/S100050010051.
- [58] J.M. Hyde, E.A. Marquis, K.B. Wilford, T.J. Williams, A sensitivity analysis of the maximum separation method for the characterisation of solute clusters, *Ultramicroscopy* 111 (2011) 440–447, doi:10.1016/j.ultramic.2010.12.015.
- [59] E.A. Jäggle, P.-P. Choi, D. Raabe, The maximum separation cluster analysis algorithm for atom-probe tomography: parameter determination and accuracy, *Microsc. Microanal.* 20 (2014) 1662–1671, doi:10.1017/S1431927614013294.
- [60] M.F. Ashby, K.E. Easterling, The transformation hardening of steel surfaces by laser beams—I. Hypo-eutectoid steels, *Acta Metall.* 32 (1984) 1935–1948, doi:10.1016/0001-6160(84)90175-5.
- [61] D. Dye, O. Hunziker, R.C. Reed, Numerical analysis of the weldability of superalloys, *Acta Mater.* 49 (2001) 683–697, doi:10.1016/S1359-6454(00)00361-X.
- [62] A. Hess, R. Schuster, A. Heider, R. Weber, T. Graf, Continuous wave laser welding of copper with combined beams at wavelengths of 1030nm and of 515nm, *Phys. Proc.* 12 (2011) 88–94, doi:10.1016/j.phpro.2011.03.012.
- [63] C.D. Boley, S.A. Khairallah, A.M. Rubenchik, Calculation of laser absorption by metal powders in additive manufacturing, *Appl. Opt.* 54 (2015) 2477–2482, doi:10.1364/AO.54.002477.
- [64] H.T. Zhou, J.W. Zhong, X. Zhou, Z.K. Zhao, Q.B. Li, Microstructure and properties of Cu–1.0Cr–0.2Zr–0.03Fe alloy, *Mater. Sci. Eng. A* 498 (2008) 225–230, doi:10.1016/j.msea.2008.07.061.
- [65] A. Chbihi, X. Sauvage, D. Blavette, Influence of plastic deformation on the precipitation of Cr in copper, *J. Mater. Sci.* 49 (2014) 6240–6247, doi:10.1007/s10853-014-8348-3.
- [66] F. Cernuschi, P.G. Bison, S. Marinetti, P. Scardi, Thermophysical, mechanical and microstructural characterization of aged free-standing plasma-sprayed zirconia coatings, *Acta Mater.* 56 (2008) 4477–4488, doi:10.1016/j.actamat.2008.04.067.
- [67] K.A. Mumtaz, P. Erasenthiran, N. Hopkinson, High density selective laser melting of Waspalloy®, *J. Mater. Process. Technol.* 195 (2008) 77–87, doi:10.1016/j.jmatprotec.2007.04.117.
- [68] J. Chen, L. Xue, S.-H. Wang, Experimental studies on process-induced morphological characteristics of macro- and microstructures in laser consolidated alloys, *J. Mater. Sci.* 46 (2011) 5859–5875, doi:10.1007/s10853-011-5543-3.
- [69] B.E. Carroll, T.A. Palmer, A.M. Beese, Anisotropic tensile behavior of Ti–6Al–4V components fabricated with directed energy deposition additive manufacturing, *Acta Mater.* 87 (2015) 309–320, doi:10.1016/j.actamat.2014.12.054.
- [70] V. Manvatkar, A. De, T. DebRoy, Spatial variation of melt pool geometry, peak temperature and solidification parameters during laser assisted additive manufacturing process, *Mater. Sci. Technol.* 31 (2015) 924–930, doi:10.1179/1743284714Y.0000000701.
- [71] M. Gäumann, S. Henry, F. Cléton, J.-D. Wagnière, W. Kurz, Epitaxial laser metal forming: analysis of microstructure formation, *Mater. Sci. Eng. A* 271 (1999) 232–241, doi:10.1016/S0921-5093(99)00202-6.
- [72] M. Gäumann, C. Bezençon, P. Canalis, W. Kurz, Single-crystal laser deposition of superalloys: processing–microstructure maps, *Acta Mater.* 49 (2001) 1051–1062, doi:10.1016/S1359-6454(00)00367-0.
- [73] G.P. Dinda, A.K. Dasgupta, J. Mazumder, Laser aided direct metal deposition of Inconel 625 superalloy: microstructural evolution and thermal stability, *Mater. Sci. Eng. A* 509 (2009) 98–104, doi:10.1016/j.msea.2009.01.009.
- [74] L. Thijs, K. Kempen, J.-P. Kruth, J. Van Humbeeck, Fine-structured aluminium products with controllable texture by selective laser melting of pre-alloyed AlSi10Mg powder, *Acta Mater.* 61 (2013) 1809–1819, doi:10.1016/j.actamat.2012.11.052.
- [75] L. Korcakova, J. Hald, M.A.J. Somers, Quantification of Laves phase particle size in 9CrW steel, *Mater. Charact.* 47 (2001) 111–117, doi:10.1016/S1044-5803(01)00159-0.
- [76] A.J. Breen, M.P. Moody, A.V. Ceguerra, B. Gault, V.J. Araullo-Peters, S.P. Ringer, Restoring the lattice of Si-based atom probe reconstructions for enhanced information on dopant positioning, *Ultramicroscopy* 159 (2015) 314–323, doi:10.1016/j.ultramic.2015.05.011.
- [77] A.J. Breen, L.T. Stephenson, B. Sun, Y. Li, O. Kasian, D. Raabe, M. Herbig, B. Gault, Solute hydrogen and deuterium observed at the near atomic scale in high-strength steel, *Acta Mater.* (2020), doi:10.1016/j.actamat.2020.02.004.
- [78] H.-W. Yen, S.W. Ooi, M. Eizadjou, A. Breen, C.-Y. Huang, H.K.D.H. Bhadeshia, S.P. Ringer, Role of stress-assisted martensite in the design of strong ultrafine-grained duplex steels, *Acta Mater.* 82 (2015) 100–114, doi:10.1016/j.actamat.2014.09.017.
- [79] B. Gault, M.P. Moody, J.M. Cairney, S.P. Ringer, *Atom Probe Microscopy*, Springer-Verlag, New York, 2012 www.springer.com/de/book/9781461434351 accessed September 6, 2018.
- [80] M.P. Moody, A.V. Ceguerra, A.J. Breen, X.Y. Cui, B. Gault, L.T. Stephenson, R.K.W. Marceau, R.C. Powles, S.P. Ringer, Atomically resolved tomography to directly inform simulations for structure–property relationships, *Nat. Commun.* 5 (2014) 1–10, doi:10.1038/ncomms6501.
- [81] C. Xia, W. Zhang, Z. Kang, Y. Jia, Y. Wu, R. Zhang, G. Xu, M. Wang, High strength and high electrical conductivity Cu–Cr system alloys manufactured

- by hot rolling–quenching process and thermomechanical treatments, *Mater. Sci. Eng. A* 538 (2012) 295–301, doi:[10.1016/j.msea.2012.01.047](https://doi.org/10.1016/j.msea.2012.01.047).
- [82] K. Zeng, M. Härmäläinen, Thermodynamic analysis of stable and metastable equilibria in the Cu–Cr system, *Calphad* 19 (1995) 93–104, doi:[10.1016/0364-5916\(95\)00010-C](https://doi.org/10.1016/0364-5916(95)00010-C).
- [83] T. Fujii, H. Nakazawa, M. Kato, U. Dahmen, Crystallography and morphology of nanosized Cr particles in a Cu–0.2% Cr alloy, *Acta Mater.* 48 (2000) 1033–1045, doi:[10.1016/S1359-6454\(99\)00411-5](https://doi.org/10.1016/S1359-6454(99)00411-5).
- [84] G.C. Weatherly, P. Humble, D. Borland, Precipitation in a Cu–0.55 wt.% Cr alloy, *Acta Metall.* 27 (1979) 1815–1828, doi:[10.1016/0001-6160\(79\)90072-5](https://doi.org/10.1016/0001-6160(79)90072-5).
- [85] W.C. Oliver, G.M. Pharr, An improved technique for determining hardness and elastic modulus using load and displacement sensing indentation experiments, *J. Mater. Res.* 7 (1992) 1564–1583, doi:[10.1557/JMR.1992.1564](https://doi.org/10.1557/JMR.1992.1564).
- [86] Y.Y. Lim, M.M. Chaudhri, The effect of the indenter load on the nanohardness of ductile metals: an experimental study on polycrystalline work-hardened and annealed oxygen-free copper, *Philos. Mag. A* 79 (1999) 2979–3000, doi:[10.1080/01418619908212037](https://doi.org/10.1080/01418619908212037).
- [87] Y.Y. Lim, M.M. Chaudhri, The influence of grain size on the indentation hardness of high-purity copper and aluminium, *Philos. Mag. A* 82 (2002) 2071–2080, doi:[10.1080/01418610208235717](https://doi.org/10.1080/01418610208235717).
- [88] S.F. Pugh, XCII. Relations between the elastic moduli and the plastic properties of polycrystalline pure metals, *Lond. Edinb. Dublin Philos. Mag. J. Sci.* 45 (1954) 823–843, doi:[10.1080/14786440808520496](https://doi.org/10.1080/14786440808520496).
- [89] D. Tabor, A simple theory of static and dynamic hardness, *Proc. R. Soc. Lond. A* 192 (1948) 247–274, doi:[10.1098/rspa.1948.0008](https://doi.org/10.1098/rspa.1948.0008).
- [90] T. Gladman, Precipitation hardening in metals, *Mater. Sci. Technol.* 15 (1999) 30–36, doi:[10.1179/026708399773002782](https://doi.org/10.1179/026708399773002782).
- [91] P. Liu, B.X. Kang, X.G. Cao, J.L. Huang, B. Yen, H.C. Gu, Aging precipitation and recrystallization of rapidly solidified Cu–Cr–Zr–Mg alloy, *Mater. Sci. Eng. A* 265 (1999) 262–267, doi:[10.1016/S0921-5093\(98\)01149-6](https://doi.org/10.1016/S0921-5093(98)01149-6).
- [92] S.I. Hong, J.S. Song, Strength and conductivity of Cu–9Fe–1.2X (X = Ag or Cr) filamentary microcomposite wires, *Metall. Mater. Trans. A* 32 (2001) 985–991, doi:[10.1007/s11661-001-0356-7](https://doi.org/10.1007/s11661-001-0356-7).
- [93] C.P. Massey, S.N. Dryepont, P.D. Edmondson, M.G. Frith, K.C. Littrell, A. Kini, B. Gault, K.A. Terrani, S.J. Zinkle, Multiscale investigations of nanoprecipitate nucleation, growth, and coarsening in annealed low-Cr oxide dispersion strengthened FeCrAl powder, *Acta Mater.* 166 (2019) 1–17, doi:[10.1016/j.actamat.2018.11.062](https://doi.org/10.1016/j.actamat.2018.11.062).
- [94] C.P. Massey, D.T. Hoelzer, R.L. Seibert, P.D. Edmondson, A. Kini, B. Gault, K.A. Terrani, S.J. Zinkle, Microstructural evaluation of a Fe–12Cr nanostructured ferritic alloy designed for impurity sequestration, *J. Nucl. Mater.* 522 (2019) 111–122, doi:[10.1016/j.jnucmat.2019.05.019](https://doi.org/10.1016/j.jnucmat.2019.05.019).
- [95] D.D. Gu, W. Meiners, K. Wissenbach, R. Poprawe, Laser additive manufacturing of metallic components: materials, processes and mechanisms, *Int. Mater. Rev.* 57 (2012) 133–164, doi:[10.1179/1743280411Y.0000000014](https://doi.org/10.1179/1743280411Y.0000000014).
- [96] V.K. Sarin, N.J. Grant, Cu–Zr and Cu–Zr–Cr alloys produced from rapidly quenched powders, *Metall. Mater. Trans. B* 3 (1972) 875–878, doi:[10.1007/BF02647661](https://doi.org/10.1007/BF02647661).
- [97] M. Bizjak, B. Karpe, G. Jakša, J. Kovač, Surface precipitation of chromium in rapidly solidified Cu–Cr alloys, *Appl. Surf. Sci.* 277 (2013) 83–87, doi:[10.1016/j.apsusc.2013.04.005](https://doi.org/10.1016/j.apsusc.2013.04.005).
- [98] A. Bachmaier, G.B. Rathmayr, M. Bartosik, D. Apel, Z. Zhang, R. Pippan, New insights on the formation of supersaturated solid solutions in the Cu–Cr system deformed by high-pressure torsion, *Acta Mater.* 69 (2014) 301–313, doi:[10.1016/j.actamat.2014.02.003](https://doi.org/10.1016/j.actamat.2014.02.003).
- [99] T.P. Harzer, S. Djaziri, R. Raghavan, G. Dehm, Nanostructure and mechanical behavior of metastable Cu–Cr thin films grown by molecular beam epitaxy, *Acta Mater.* 83 (2015) 318–332, doi:[10.1016/j.actamat.2014.10.013](https://doi.org/10.1016/j.actamat.2014.10.013).
- [100] D.L.M. Ellis, Mechanical and Thermal Properties of Two Cu–Cr–Nb Alloys and NARloy-Z, 1996. <https://ntrs.nasa.gov/search.jsp?R=19970002915> (accessed November 10, 2017).
- [101] D.J. Chakrabarti, D.E. Laughlin, The Cr–Cu (chromium–copper) system, *Bull. Alloy Phase Diagr.* 5 (1984) 59–68, doi:[10.1007/BF02868727](https://doi.org/10.1007/BF02868727).
- [102] W. Xu, E.W. Lui, A. Pateras, M. Qian, M. Brandt, In situ tailoring microstructure in additively manufactured Ti–6Al–4V for superior mechanical performance, *Acta Mater.* 125 (2017) 390–400, doi:[10.1016/j.actamat.2016.12.027](https://doi.org/10.1016/j.actamat.2016.12.027).
- [103] H. Mohseni, P. Nandwana, A. Tsoi, R. Banerjee, T.W. Scharf, In situ nitrided titanium alloys: microstructural evolution during solidification and wear, *Acta Mater.* 83 (2015) 61–74, doi:[10.1016/j.actamat.2014.09.026](https://doi.org/10.1016/j.actamat.2014.09.026).
- [104] Q. Jia, P. Rometsch, P. Kürsteiner, Q. Chao, A. Huang, M. Weyland, L. Bourgeois, X. Wu, Selective laser melting of a high strength AlMnSc alloy: alloy design and strengthening mechanisms, *Acta Mater.* 171 (2019) 108–118, doi:[10.1016/j.actamat.2019.04.014](https://doi.org/10.1016/j.actamat.2019.04.014).
- [105] C.T. Kwok (Ed.), *Laser Surface Modification of Alloys for Corrosion and Erosion Resistance*, Woodhead Publishing, 2012 <https://www.elsevier.com/books/laser-surface-modification-of-alloys-for-corrosion-and-erosion-resistance/kwok/978-0-85709-015-7> accessed April 23, 2020.